mathematics

Article

Insights into the 3D Slip Dynamics of Jeffrey Fluid Due to a Rotating Disk with Exponential Space-Dependent Heat Generation: A Case Involving a Non-Fourier Heat Flux Model

Ali Saleh Alshomrani

Mathematical Modelling and Applied Computation (MMAC) Research Group, Department of Mathematics, Faculty of Science, King Abdulaziz University, P.O. Box 80203, Jeddah 21589, Saudi Arabia; aszalshomrani@kau.edu.sa

Abstract: The dynamics of non-Newtonian Jeffrey fluid in conjunction with a spinning disk surface can be problematic in heating systems, polymer technology, microelectronics, advanced technology, and substantive disciplines. Therefore, the significance of the Hall current and Coriolis forces in terms of the dynamics of Jeffrey fluid flowing across a gyrating disk subject to non-Fourier heat flux was investigated in this study. A temperature-related heat source (TRHS) and exponential-related heat source (ERHS) were incorporated into the model to improve the thermal characteristics. Thermal radiation and multiple slip effects were employed in the flow system. The connected non-linear PDEs governing the transport were transmuted into non-linear ODEs and solved using the Runge–Kutta shooting technique (RKST). The results of the RKST were substantiated in previous studies and found to have adequate reliability. The numerical values of the coefficient of friction and the Nusselt number were simulated. The non-Fourier heat flux was found to have a higher rate of heat transfer (HTR) than with traditional Fourier heat flux. Furthermore, both TRHS and ERHS phenomena support the progression of HTR. The swelling effects of the Hall current influence the velocities, whilst the temperature of the Jeffrey fluid shows the opposite tendency. Furthermore, asymptotic variances were detected for larger Hall parameter values.

Keywords: Jeffrey fluid; rotating disk; thermal radiation; Hall current; exponential dependent heat source; Cattaneo–Christov heat flux

MSC: 76A02; 76A05

Citation: Alshomrani, A.S. Insights into the 3D Slip Dynamics of Jeffrey Fluid Due to a Rotating Disk with Exponential Space-Dependent Heat Generation: A Case Involving a Non-Fourier Heat Flux Model. *Mathematics* **2023**, *11*, 1096. https://doi.org/10.3390/math11051096

Academic Editors: Katta Ramesh and Rama Subba Reddy Gorla

Received: 24 January 2023
Revised: 15 February 2023
Accepted: 16 February 2023
Published: 22 February 2023

1. Introduction

The rotational flow problems created by spinning discs are of considerable interest because of their relevance to industry and technology. The von Kármán problem [1] concerns the dynamics of viscous fluid associated with infinite revolving disks. The von Kármán problem can be applied to gas turbine rotors, electronic devices, rotating machines, medical devices, crystal growth processes, rotating heat exchangers, storage devices, etc. Relevant applications and studies of disk flows have been reported by Brady and Durlofsky [2], Cobb and Saunders [3], Benton [4], and Tribollet and Newman [5]. Turkyilmazoglu [6] extended [1] by exploring heat transfer using a nanoliquid as the test fluid and stated that more torque is needed to ensure stable rotation of the disc. Considering an oscillating extensible disk, Ellahi [7] examined the effect of a rotating disk on the dynamics of a nano-ferroliquid. The consequences of slip conditions at the revolving disk surface in terms of the flow of magnetized nanofluid were studied by Hayat et al. [8], who reported that slip conditions control the growth of disk surface layer width. Aziz et al. [9] investigated the effects of internal thermal source/sink on nanoliquid transition, and they concluded that an internal thermal source causes an increase in heat transfer inside the nanoliquid system. According to Mahanthesh et al. [10], as compared to temperature-related thermal generation, exponential space-related internal thermal generation has a greater impact on the surface thermal layer. Mahanthesh et al. also discussed the Lorentz and Coriolis forces and their effects on the dynamics of magnetized fluid.

Cowling [11] has argued that in order to create a strong enough magnetic force, Ohm's law must be considerable for Hall currents. Hall effects are crucial in low-electron-density and strong magnetism scenarios because it is highly likely that the rheological behavior of the (ionized) liquid will be modified. The effect of the Hall current on von Kármán's rotating flow was analyzed by Aboul-Hassan and Attia [12], who reported that the Hall effects would allow the rotational flux to stabilize. Acharya et al. [13] performed numerical treatment of the radiative flux guided by the Hall current and the Coriolis force. Considering the porous matrix in the disk, Maleque and Sattar [14] discussed the implications of the Hall current for disk flux. Hall current stimulation and variable fluid conductivity/viscosity in disk-driven dynamics were examined by Abdel-Wahed and Akl [15], involving kinetic energy and the effects of non-linear radiation. Shaheen et al. [16] also examined the characteristics of the Hall current in the flow of Casson material across a disk. Shehzad et al. [17] investigated stimulation of the Hall current on the surface of an oscillating disk with varying liquid density. Hayat et al. [18] examined Hall effects on flow using a non-coaxial spinning disk with unstable effects. Maleque [19] studied the space- and temperature-related effects of viscosity on flow guided by the Hall current with an unstable rotating disk. Turkyilmazoglu [20] provided the exact solution to the von Kármán problem for the Hall current and the nanofluid. Many researchers [21–30] have studied the relationship between magnetic fields and the dynamics of fluid subjected to various physical configurations and applications.

It should be noted that the kinetic and thermal properties of non-Newtonian Jeffrey fluid propelled by a gyrating disk have not been fully defined. Jeffrey fluids can be used in materials processing, food processing, chemical processing, polymer engineering, and other fields. A Jeffrey fluid model can provide data on relaxation time and delay. Qasim [31] exploited the stretching sheet problem for Jeffrey fluid with thermal mass transport effects under a heat sink. Reddy and Makinde [32] explored the problem of peristaltic transport of Jeffrey fluid by considering magnetized nanoparticles using analytical tools. Sandeep et al. [33] studied the stagnation flow problem associated with Jeffrey fluid, considering the induced magnetic field, the stretch sheet, and the chemical reaction. Mehmood et al. [34] examined the oblique flow problem for Jeffrey fluid carrying magnetic nanoparticles, taking into account plate elongation and heat transport. Saleem et al. [35] studied the rotating cone problem using Jeffrey fluid subject to chemical reactions, magnetic transport, convective heat conditions, and heat source effects. Khan et al. [36] presented rough, semi-analytical solutions for the revised stagnation flow problem using an off-center spinning disk with Jeffrey fluid. Farooq et al. [37] reported the 3D flow of Jeffrey magnetic fluid in an elastic cylinder, with Newtonian heating and magnetism. Hayat et al. [38] explored the non-linear flow of Jeffrey fluid on two gyrating disk surfaces subjected to two chemical reactions and radiation. Several investigations have been conducted into transport of Jeffrey liquid between two revolving disk surfaces, among others, those by Reddy et al. [39], Hayat et al. [40,41], Muhammad et al. [42], and Kumar and Kavitha [43]. Studying Jeffrey fluid on the spinning disk surface, Hayat et al. [44] performed flow analysis with MHD effects, Siddiqui et al. [45] revisited the von Kármán problem, Qasim et al. [46] performed 2D heat transport with variable conductivity and radioactive features, Sadiq et al. [47] conducted flow analysis, Imtiaz et al. [48] scrutinized two varieties of chemical reactions and non-Fourier thermal flux effects, and Sadiq [49] investigated lubrication effects. However, little is known about the heat transport characteristics of Jeffrey fluid transport caused by the revolving disk.

The studies cited above were restricted to the classical Fourier heat flux model [50], which disregards thermal relaxation properties. Cattaneo [51] expanded Fourier's [50] concept by taking thermal relaxation time properties into account using a hyperbolic model. Christov [52] then applied Cattaneo's model [51], taking the Oldroyd upper convected derivative into account. A comprehensive Cattaneo–Christov thermal-flow model (CCTFM) has been implemented in numerous experiments. Bissell [53] employed the Cattaneo–Christov thermal flux model (CCTFM) to examine the thermal convection of a magnetized fluid. Layek and Pati [54] examined the features of CCTFM in convection with bifurcation and chaos aspects. Mehmood et al. [55] explored the CCTFM features of oblique stagnation transport using magnetized Oldroyd-B fluid subjected to a chemical reaction. Shamshuddin et al. [56] evaluated CCTFM features of swirling thermal convection between co-axial revolving disks using a perturbation method. Mabood et al. [57] examined the CCTFM features of the transport of Sutterby fluid on a revolving elongated disk. Sampath Kumar et al. [58] studied the CCTFM features of Jeffrey nanofluid on a stretchable plate subjected to quadratic convection and linear radiation numerically. Recently, Hayat et al. [59] explored the CCTFM features of Jeffrey fluid on a revolving disk with changeable heat conductivity.

Some studies in the literature have observed the CCTFM (Cattaneo–Christov thermal flux model) features of Jeffrey fluid on a revolving disk, taking into account the effects of the Hall current, exponential-related thermal source (ERTS), temperature-related thermal source (TRTS), and multiple slippages. To the best of our knowledge, none of the above-mentioned research has studied the issue at hand in depth. As a result, the primary goal of this research was to make use of the CCTFM characteristics of Jeffrey fluid movement generated by a rotating disk surface subjected to an ERTS and TRTS. The coupled non-linear PDEs that regulate transport were converted into non-linear ODEs and solved using the Runge–Kutta shooting approach (RKST). The RKST results were validated using the findings of prior investigations, and the reliability of the RKST results was confirmed. The coefficient of friction and the Nusselt number were simulated, tabulated, and analyzed numerically. The following research questions were investigated in this study:

- What influence do the Deborah number, Hall effect, and magnetic field have on the hydrodynamics of the Jeffrey fluid surface layer under first-order slip conditions?
- How do CCTFM characteristics affect heat transport features under thermal slip conditions?
- What effect do the ERTS and TRTS parameters have on the temperature and the Nusselt number?
- What effect does the Deborah number have on the friction factors?

2. Formulation of the Problem

Transmission of the Jeffrey fluid occurred across an infinite revolving disk at $z = 0$, rotating with angular velocity Ω (see Figure 1). The density (ρ), electrical conductivity (σ), thermal conductivity (k), specific heat (ρC_p), kinematic viscosity (υ), and dynamic viscosity (μ) were non-altering properties. The Hall current was subject to a solid magnetic field along the z direction, as modeled by [11]:

$$\boldsymbol{J} + \frac{\omega_e \tau_e}{B_0}(\boldsymbol{J} \times \boldsymbol{B}) = \sigma\left(\boldsymbol{E} + \boldsymbol{V} \times \boldsymbol{B} + \frac{\nabla P_e}{e\eta_e}\right), \tag{1}$$

where ω_e is the electron frequency, $\boldsymbol{V}$ is the velocity vector, τ_e is the electron collision time, $\boldsymbol{J}$ is the current density, P_e is the electron pressure, $\boldsymbol{B}$ is the magnetic field $(0, 0, B_0)$, B_0 is the intensity of the magnetic field, e is the electron charge, $\boldsymbol{E}$ is the electric field, and η_e is the electron number density. The following assumptions were made in the analysis:

- The flow is laminar, steady, and axisymmetric.
- The fluid is incompressible, meaning that the density of the fluid is taken to be constant.
- Fluid properties are kept constant.
- The first-order velocity slip and temperature jump conditions are incorporated on the disk surface, whereas the velocity and temperature are kept constant in an ambient state.

- The Cattaneo–Christov heat flux (CCHF) model for temperature is used.
- The electric field, ion slip, and polarization effects are ignored.

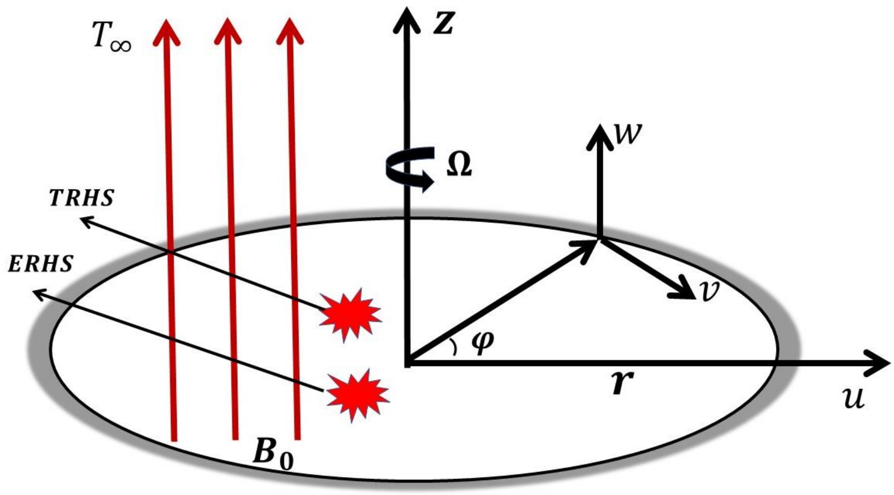

Figure 1. Physical configuration of the problem.

Let us assume Rosseland's radiative heat flux q_r (see [15]), as follows:

$$q_r = -\frac{4\sigma^*}{3k^*}\nabla T^4, \tag{2}$$

where T is the temperature, σ^* is the Stefan–Boltzmann factor, and k^* is Rosseland's mean absorption. Since the Jeffrey fluid is optically thick, Rosseland's radiation approximation is well suited. The Jeffrey fluid's constitutive equation is (see [44])

$$\boldsymbol{\tau} = -p\boldsymbol{I} + \boldsymbol{S}, \tag{3}$$

$$\boldsymbol{S} = \frac{\mu}{1+\alpha}\left(\dot{\boldsymbol{r}} + \lambda_1\ddot{\boldsymbol{r}}\right), \tag{4}$$

where p is the pressure, $\boldsymbol{I}$ is the identity tensor, $\boldsymbol{S}$ is the extra stress tensor, α is the ratio of relaxation time to retardation time, and λ_1 is the retardation time. Variables $\dot{\boldsymbol{r}}$ and $\ddot{\boldsymbol{r}}$ are

$$\dot{\boldsymbol{r}} = \nabla\boldsymbol{V} + transpose(\nabla\boldsymbol{V}), \tag{5}$$

$$\ddot{\boldsymbol{r}} = \frac{D}{Dt}(\dot{\boldsymbol{r}}) = \frac{\partial}{\partial t}(\dot{\boldsymbol{r}}) + (\boldsymbol{V}\cdot\nabla)\dot{\boldsymbol{r}}, \tag{6}$$

where $\frac{D}{Dt}$ is the material derivative. The frame of the cylindrical coordinate $(r,\ \varphi, z)$ is chosen accordingly. The velocities are to be $(u,\ v,\ w)$. The pertinent non-linear boundary-layer axisymmetric PDEs governing the heat transport of Jeffrey fluid are (see [44])

$$\frac{\partial u}{\partial r} + \frac{u}{r} + \frac{\partial w}{\partial z} = 0, \tag{7}$$

$$\begin{aligned} u\frac{\partial u}{\partial r} + w\frac{\partial u}{\partial z} - \frac{v^2}{r} = \frac{\nu}{1+\alpha}\left[\frac{\partial^2 u}{\partial z^2} + \lambda_1\left(\frac{\partial u}{\partial z}\frac{\partial^2 u}{\partial r\partial z} + u\frac{\partial^3 u}{\partial r\partial z^2} + \frac{\partial w}{\partial z}\frac{\partial^2 u}{\partial z^2}\right)\right] - \frac{\sigma B_0^2}{1+m^2}(u - mv) \\ + \frac{\nu\lambda_1}{1+\alpha}\left[w\frac{\partial^3 u}{\partial z^3} - \frac{1}{r}\left(\frac{\partial v}{\partial z}\right)^2 - \frac{v}{r}\frac{\partial^2 v}{\partial z^2}\right], \end{aligned} \tag{8}$$

$$u\frac{\partial v}{\partial r}+w\frac{\partial v}{\partial z}+\frac{uv}{r}=\frac{v}{1+\alpha}\left[\frac{\partial^2 v}{\partial z^2}+\lambda_1\left(\frac{\partial u}{\partial z}\frac{\partial^2 v}{\partial r\partial z}+u\frac{\partial^3 v}{\partial r\partial z^2}+\frac{\partial w}{\partial z}\frac{\partial^2 v}{\partial z^2}\right)\right]-\frac{\sigma B_0^2}{1+m^2}(v+mu)$$
$$+\frac{v\lambda_1}{1+\alpha}\left[w\frac{\partial^3 v}{\partial z^3}+\frac{1}{r}\frac{\partial u}{\partial z}\frac{\partial v}{\partial z}+\frac{v}{r}\frac{\partial^2 u}{\partial z^2}\right], \tag{9}$$

$$\rho C_p\left(u\frac{\partial T}{\partial r}+w\frac{\partial T}{\partial z}\right)=-\nabla\cdot\boldsymbol{q}+\frac{16\sigma^* T_\infty^3}{3k^*}\frac{\partial^2 T}{\partial z^2}+q_t(T-T_\infty)+q_e(T_w-T_\infty)\exp\left(-n\sqrt{\frac{2\Omega}{v}}\right), \tag{10}$$

where T_∞ is the ambient temperature, $m=\omega_e\tau_e$ is the dimensionless Hall factor, q_t and q_e are the TRTS and ERTS coefficients, respectively, T_w and T_∞ are surface and ambient temperature, respectively, and n is the exponential index. The CCHF is presented as in [50–55]:

$$\boldsymbol{q}+\lambda_2\left(\frac{\partial \boldsymbol{q}}{\partial t}+(\nabla\cdot\boldsymbol{V})\boldsymbol{q}+\boldsymbol{V}\cdot\nabla\boldsymbol{q}-\boldsymbol{q}\cdot\nabla\boldsymbol{V}\right)=-k\nabla T. \tag{11}$$

For time-independent and constant density fluid, we have

$$\boldsymbol{q}+\lambda_2(\boldsymbol{V}\cdot\nabla\boldsymbol{q}-\boldsymbol{q}\cdot\nabla\boldsymbol{V})=-k\nabla T. \tag{12}$$

In view of (12), Equation (10) yields

$$\rho C_p\left(u\frac{\partial T}{\partial r}+w\frac{\partial T}{\partial z}\right)=k\frac{\partial^2 T}{\partial z^2}+\frac{16\sigma^* T_\infty^3}{3k^*}\frac{\partial^2 T}{\partial z^2}+q_t(T-T_\infty)+q_e(T_w-T_\infty)\exp\left(-n\sqrt{\frac{2\Omega}{v}}\right)$$
$$-\lambda_2\left[w^2\frac{\partial^2 T}{\partial z^2}+u^2\frac{\partial^2 T}{\partial r^2}+2uw\frac{\partial^2 T}{\partial r\partial z}+\frac{\partial T}{\partial r}\left(u\frac{\partial u}{\partial r}+w\frac{\partial u}{\partial z}\right)+\frac{\partial T}{\partial z}\left(u\frac{\partial w}{\partial r}+w\frac{\partial w}{\partial z}\right)\right]. \tag{13}$$

Apposite boundary conditions are (see [41,45])

$$u=L_1\frac{\partial u}{\partial z},\quad v=r\Omega+L_1\frac{\partial v}{\partial z},\quad w=0,\quad T=T_w+L_2\frac{\partial T}{\partial z},\quad \text{at}\quad z=0, \tag{14}$$

$$u\to 0,\quad v\to 0,\quad T\to T_\infty,\quad \text{as}\quad z\to\infty, \tag{15}$$

where L_1 and L_1 are the velocity and temperature slip coefficients, respectively.

By using the appropriate transformations [6–8],

$$\xi=z\sqrt{\frac{2\Omega}{v}},\quad f'(\xi)=\frac{u(r,z)}{r\Omega},\quad g(\xi)=\frac{v(r,z)}{r\Omega},$$
$$f(\xi)=\frac{w(r,z)}{-\sqrt{2\Omega v}},\qquad \theta(\xi)=\frac{T-T_\infty}{T_w-T_\infty}, \tag{16}$$

where ξ, $f'(\xi)$, $g(\xi)$, $f(\xi)$, and θ are the dimensionless similarity variable, radial velocity, tangential velocity, axial velocity, and temperature, respectively.

Taking Equation (16) and applying it to Equations (8), (9), and (13) yields

$$f'''-\frac{Ha(1+\alpha)}{2(1+m^2)}(f'-mg)+\frac{(1+\alpha)}{2}\left[2ff''-f'^2+g^2\right]$$
$$+\beta\left[f''^2-f'f'''-2ff''''-g'^2-gg''\right]=0, \tag{17}$$

$$g''-\frac{Ha(1+\alpha)}{2(1+m^2)}(f'-mg)+\frac{(1+\alpha)}{2}[fg'-f'g]$$
$$+\beta[2f''g'-f'g''-2fg'''+f'''g]=0, \tag{18}$$

$$\frac{1+R}{Pr}\theta''+f\theta'-2\Gamma\left(f^2\theta''+ff'\theta'\right)+Qt\theta+Qe\exp(-n\xi)=0, \tag{19}$$

$$f(\xi)=0,\ \ f'(\xi)=\delta f''(\xi),\ \ g(\xi)=1+\delta g'(\xi),\ \ \theta(\xi)=1+\zeta\theta'(\xi),\ \text{at}\ \xi=0, \tag{20}$$

$$f'(\xi)\to 0,\quad g(\xi)\to 0,\quad \theta(\xi)\to 0\ \text{ as}\ \xi\to\infty, \tag{21}$$

where $M=\frac{\sigma B_0^2}{\rho\Omega}$ denotes the magnetic parameter, $R=\frac{4\sigma^* T_\infty^3}{kk^*}$ denotes the radiation parameter, $Pr=\frac{\mu C_p}{k}$ denotes the Prandtl number, $Qt=\frac{q_t}{\mu C_p\Omega}$ denotes the TRTS parameter, $Qe=\frac{q_e}{\mu C_p\Omega}$ denotes the ERTS parameter, $\Gamma=\lambda_2\Omega$ denotes the dimensionless thermal relaxation time, $\delta=L_1\sqrt{\frac{2\Omega}{v}}$ denotes the velocity slip parameter, $\zeta=L_2\sqrt{\frac{2\Omega}{v}}$ denotes the thermal slip parameter, and $\beta=\lambda_1\Omega$ denotes the Deborah number.

The total heat flux and shear stress in the tangential and radial directions are given by

$$q_w=\left[-k\frac{\partial T}{\partial z}+q_r\right]_{z=0}, \tag{22}$$

$$\tau_\varphi=\frac{\mu}{1+\alpha}\left[\frac{\partial v}{\partial z}+\lambda_1\left(\frac{\partial v}{\partial r}\frac{\partial u}{\partial z}-2\frac{v}{r}\frac{\partial u}{\partial z}+\frac{3u}{r}\frac{\partial v}{\partial z}\right)\right], \tag{23}$$

$$\tau_r=\frac{\mu}{1+\alpha}\left[\frac{\partial u}{\partial z}+\lambda_1\left(3\frac{\partial u}{\partial r}\frac{\partial u}{\partial z}+2\frac{\partial v}{\partial r}\frac{\partial v}{\partial z}-\frac{v}{r}\frac{\partial v}{\partial z}+\frac{\partial w}{\partial z}\frac{\partial u}{\partial z}\right)\right]. \tag{24}$$

The local Nusselt number (Nu) and coefficients of wall friction in tangential (C_g) and radial (C_f) directions are given below.

$$Nu=\frac{rq_w}{k(T_w-T_\infty)}, \tag{25}$$

$$C_g=\frac{\tau_\varphi}{\rho(r\Omega)^2}, \tag{26}$$

$$C_f=\frac{\tau_r}{\rho(r\Omega)^2}, \tag{27}$$

Taking (16) and (22)–(24) and applying these to (25)–(27) yields the following:

$$\left(\frac{Re_r}{2}\right)^{-1/2}Nu=-(1+R)\theta'(0), \tag{28}$$

$$\left(\frac{Re_r}{2}\right)^{\frac{1}{2}}C_f=\frac{1}{1+\alpha}\left[f''(0)+3\beta g'(0)\right], \tag{29}$$

$$\left(\frac{Re_r}{2}\right)^{\frac{1}{2}}C_g=\frac{1}{1+\alpha}\left[g'(0)-\beta f''(0)\right], \tag{30}$$

where $Re_r=\frac{\Omega r^2}{v}$ denotes the local Reynolds number.

3. Numerical Approach

The Runge–Kutta shooting method (RKSM) was employed to solve the normalized non-linear Equations (17)–(19), subjected to (20) and (21), as follows:

$$(\mathcal{Z}_1,\ \mathcal{Z}_2,\ \mathcal{Z}_3,\ \mathcal{Z}_4,\mathcal{Z}_5,\ \mathcal{Z}_6,\ \mathcal{Z}_7,\ \mathcal{Z}_8,\mathcal{Z}_9)=\left(f,f',f'',f''',g,g',g'',\theta,\ \theta'\right),$$

to yield an IVP (initial value problem) from Equations (17)–(21):

$$\mathcal{Z}_1'=\mathcal{Z}_2, \tag{31}$$

$$\mathcal{Z}_2'=\mathcal{Z}_3, \tag{32}$$

$$\mathcal{Z}_3'=\mathcal{Z}_4, \tag{33}$$

$$\mathcal{Z}_4' = \begin{bmatrix} \mathcal{Z}_4 + \frac{1+\alpha}{2}\left(2\mathcal{Z}_1\mathcal{Z}_3 - \mathcal{Z}_2^2 + \mathcal{Z}_5^2\right) - \frac{Ha(1+\alpha)}{2(1+m^2)}\left(\mathcal{Z}_2 - m\mathcal{Z}_5\right) \\ +\beta\left(\mathcal{Z}_3^2 - \mathcal{Z}_2\mathcal{Z}_4 - \mathcal{Z}_6^2 - \mathcal{Z}_5\mathcal{Z}_7\right) \end{bmatrix} / 2\beta\mathcal{Z}_1, \quad (34)$$

$$\mathcal{Z}_5' = \mathcal{Z}_6, \quad (35)$$

$$\mathcal{Z}_6' = \mathcal{Z}_7, \quad (36)$$

$$\mathcal{Z}_7' = \begin{bmatrix} \mathcal{Z}_7 + (1+\alpha)(\mathcal{Z}_1\mathcal{Z}_6 - \mathcal{Z}_5\mathcal{Z}_2) - \frac{Ha(1+\alpha)}{2(1+m^2)}(\mathcal{Z}_5 + m\mathcal{Z}_2) \\ +\beta(2\mathcal{Z}_3\mathcal{Z}_6 - \mathcal{Z}_2\mathcal{Z}_7 + \mathcal{Z}_5\mathcal{Z}_4) \end{bmatrix} / 2\beta\mathcal{Z}_1, \quad (37)$$

$$\mathcal{Z}_8' = \mathcal{Z}_7, \quad (38)$$

$$\mathcal{Z}_9' = -\left(\frac{Pr}{1 + R - 2Pr\Gamma\mathcal{Z}_1^2}\right)\left(\mathcal{Z}_1\mathcal{Z}_9 - 2\Gamma\mathcal{Z}_1\mathcal{Z}_2\mathcal{Z}_9 + Qt\mathcal{Z}_8 + Qe\exp(-n\xi)\right). \quad (39)$$

The initial conditions were chosen and set using the classical Runge–Kutta method with an error tolerance of 10^{-8} and step size of 0.001. The initial estimates were then refined using the Newton–Raphson iterative method, such that the obtained solution satisfied the conditions at infinity. The error tolerance for the convergence criteria of the Newton–Raphson method was set to 10^{-6}. We developed an in-house MATLAB code for the computations, and the obtained solutions were validated by referring to earlier works. The results of the present study were compared with those of Hayat et al. [44], where $R = m = \delta = \zeta = \Gamma = Qt = Qe = 0$, $\alpha = 1$, and $\beta = 0.25$ (see Table 1), and this indicated good agreement.

Table 1. Comparison of $(\frac{Re_r}{2})^{\frac{1}{2}} C_f$ and $(\frac{Re_r}{2})^{\frac{1}{2}} C_g$ values for different values of Ha with those of Hayat et al. [44], where $R = m = \delta = \zeta = \Gamma = Qt = Qe = 0$, $\alpha = 1$, and $\beta = 0.25$.

Ha	**Hayat et al. [44]**		**Present Results**	
	$(\frac{Re_r}{2})^{\frac{1}{2}} C_f$	$(\frac{Re_r}{2})^{\frac{1}{2}} C_g$	$(\frac{Re_r}{2})^{\frac{1}{2}} C_f$	$(\frac{Re_r}{2})^{\frac{1}{2}} C_g$
0	1.01735	−1.27135	1.017349	−1.271352
1.0	−0.01336	−1.09247	−0.013357	−1.092468
2.0	−0.72170	−1.00951	−0.721704	−1.009513
2.5	−0.98025	−0.99714	−0.980251	−0.997145

4. Results and Discussion

This section describes the impact of Hall current and Cattaneo–Christov heat flux on the mechanisms of Jeffrey fluid on a spinning disk when thermal radiation, multiple slip conditions, an exponential-related heat source (ERHS), and temperature-related heat source (TRHS) are significant. The effects of the relaxation–retardation time ratio (α), Deborah number (β), dimensionless thermal relaxation time (Γ), Hartmann number (Ha), thermal radiation parameter (R), Hall parameter (m), velocity slip number (δ), thermal slip number (ζ), TRHS number (Qt), and ERHS number (Qe) on the self-similar radial velocity ($f'(\xi)$), azimuth velocity ($g(\xi)$), axial velocity ($f(\xi)$), and temperature ($\theta(\xi)$) are shown in Figures 2–22. Factors of technological interest, namely the Nusselt number ($(\frac{Re_r}{2})^{-\frac{1}{2}} Nu$), radial shear stress ($(\frac{Re_r}{2})^{\frac{1}{2}} C_f$), and tangential shear stress ($(\frac{Re_r}{2})^{\frac{1}{2}} C_g$), were also scrutinized. The predefined values for the relevant parameters were as follows : $R = Ha = 0.5$, $\alpha = \beta = 0.2$, $\delta = \zeta = 0.5$, $\Gamma = 0.1$, $Qt = Qe = 0.2$, $Pr = 6$, and $n = 1$.

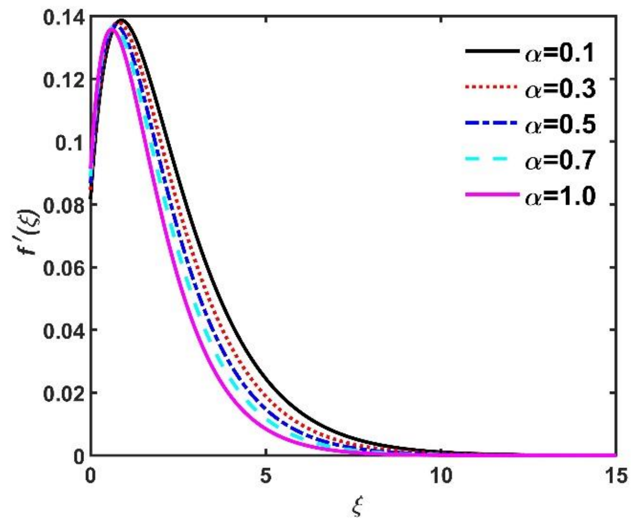

Figure 2. Impact of α on $f'(\xi)$.

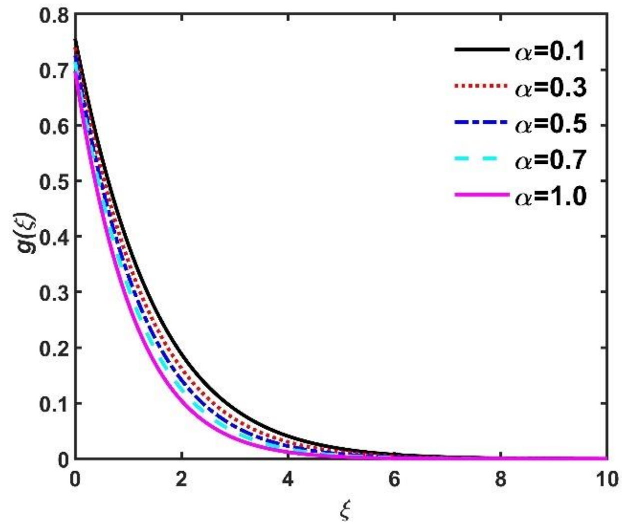

Figure 3. Impact of α on $g(\xi)$.

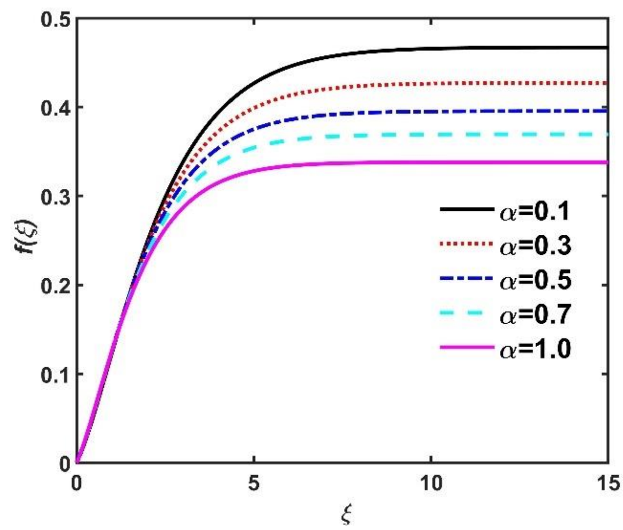

Figure 4. Impact of α on $f(\xi)$.

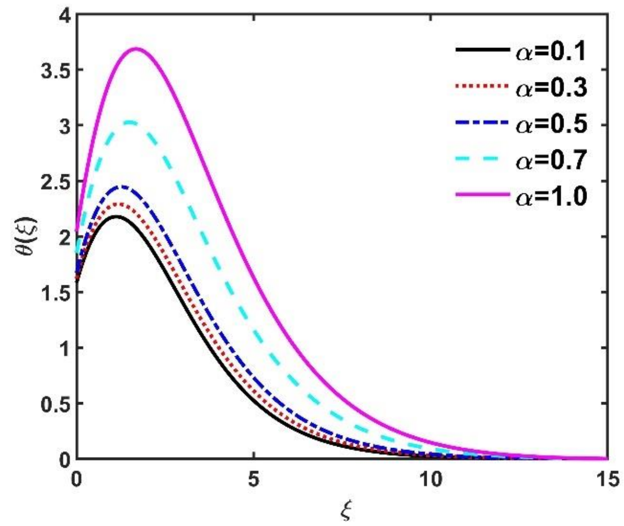

Figure 5. Impact of α on $\theta(\xi)$.

Figures 2–5 exemplify the radial velocity ($f'(\xi)$), azimuth velocity ($g(\xi)$), axial velocity ($f(\xi)$), and temperature ($\theta(\xi)$) for several values of the relaxation time–retardation time ratio (α). As the values of α increase, the retardation time lessens, meaning that Jeffrey fluid molecules need more time to achieve a state of equilibrium after being in a perturbed state. Because of this, a decrease in the momentum of the surface layer in the axial (z), azimuth (φ), and radial (r) directions was observed. Significant expansion of the temperature surface layer width was observed (shown in Figure 5) by increasing the magnitude of α from 0.1 (a relatively small value) to 1.0 (a relatively high value). The reason for this is that a longer relaxation time leads to an increase in the Jeffrey fluid temperature ($\theta(\xi)$). Figure 6 shows the radial velocity ($f'(\xi)$) when varying β, where the performance was found to improve twofold. That is, in the vicinity of the disk surface, radial velocity $f'(\xi)$ condensed, augmenting the β values, whereas the radial velocity $f'(\xi)$ remained unchanged in the rest of the flow domain. The radial velocity profile showed dual behavior with variation of β. This is because the Coriolis force exerted by the rotation of the disk leads to radial outward flow in the vicinity of the disk. When nearing an ambient state, radial velocity approaches zero, with a crossover in the middle of the flow region. The Deborah number (β) and retardation time are directly proportional, so $f'(\xi)$ is enhanced with β. In Figure 7, it is evident that the azimuth velocity ($g(\xi)$) lessens for cumulative values of β. However, in Figure 8, axial momentum ($f(\xi)$) can be seen to exhibit a contrasting relationship. Figure 9 shows that the Deborah number causes the temperature of the Jeffrey fluid to rise significantly for cumulative values of β.

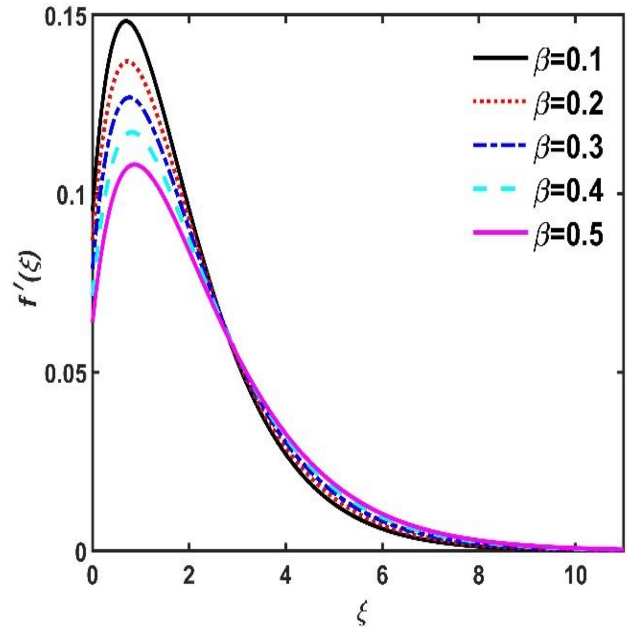

Figure 6. Impact of β on $f'(\xi)$.

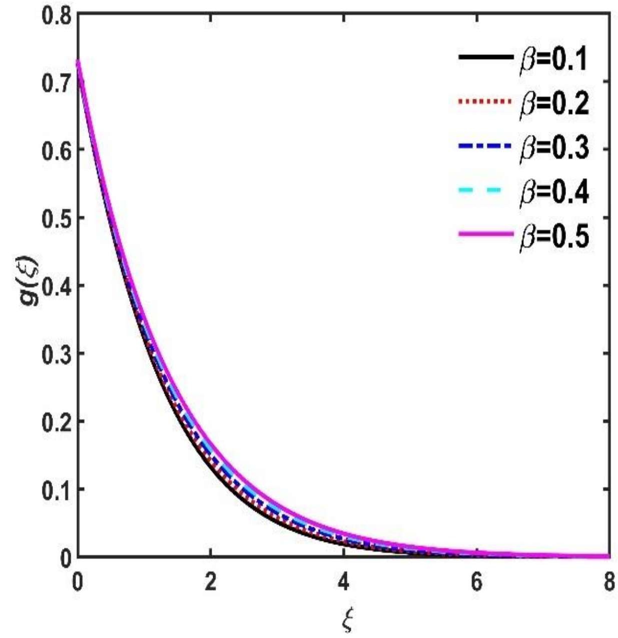

Figure 7. Impact of β on $g(\xi)$.

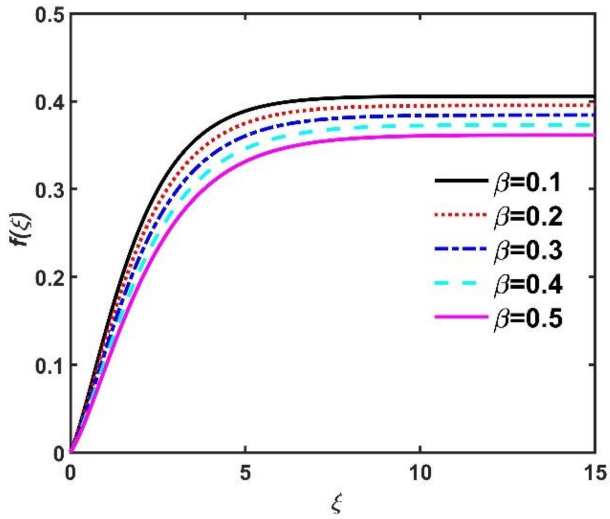

Figure 8. Impact of β on $f(\xi)$.

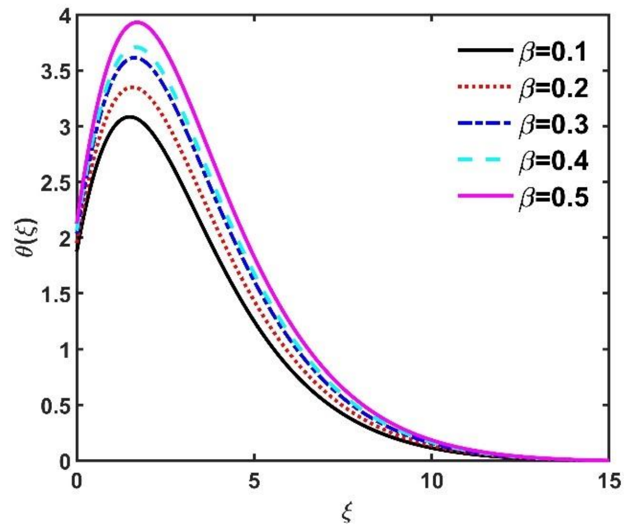

Figure 9. Impact of β on $\theta(\xi)$.

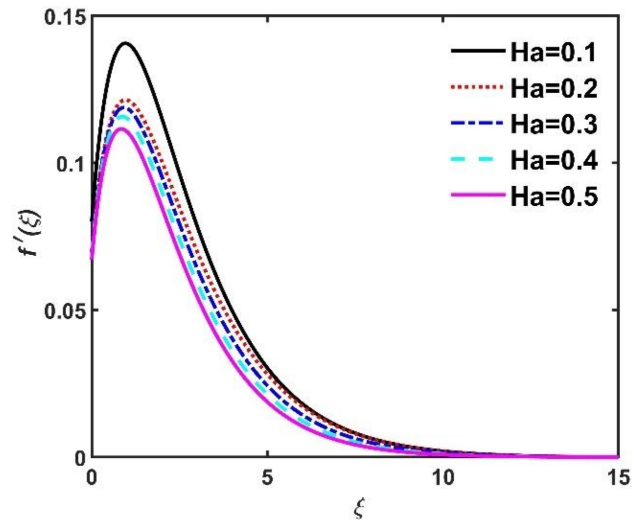

Figure 10. Impact of Ha on $f'(\xi)$.

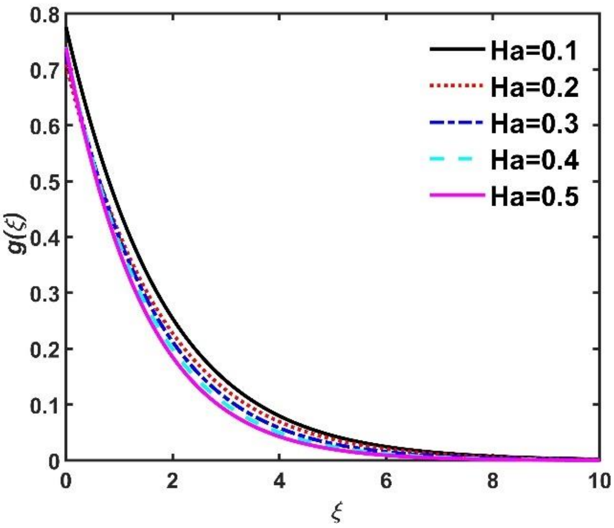

Figure 11. Impact of Ha on $g(\xi)$.

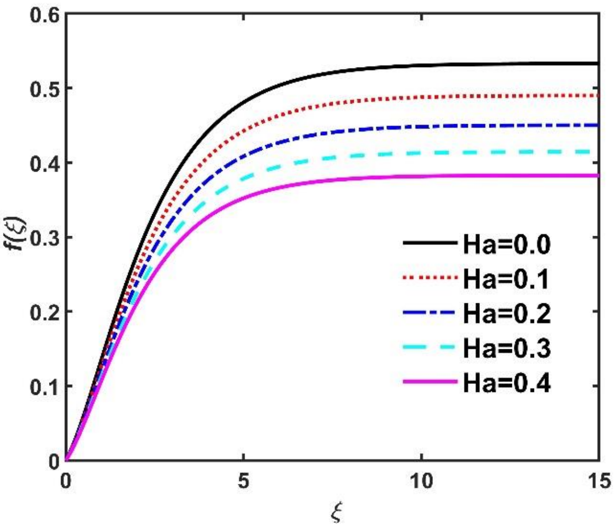

Figure 12. Impact of Ha on $f(\xi)$.

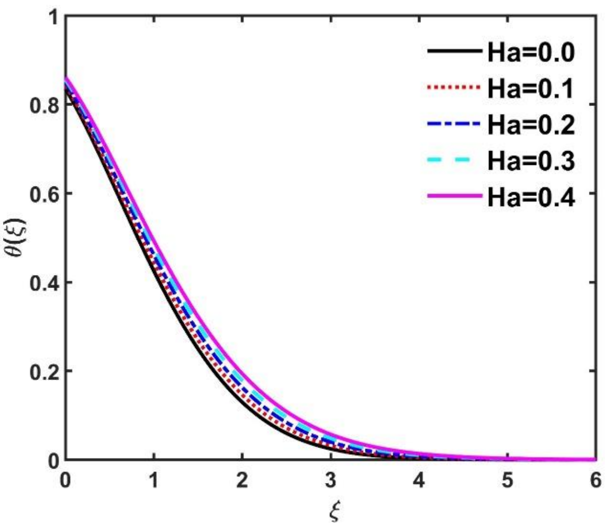

Figure 13. Impact of Ha on $\theta(\xi)$.

Frictional forces exerted by the Lorentz effect are instigated by amalgamation of a stimulating external magnetization, lessening the growth of velocities in all three directions (axial (z), azimuth (φ), and radial (r)). This is supported by Figures 10–12, which show that radial velocity ($f'(\xi)$), azimuth velocity ($g(\xi)$), and axial velocity ($f(\xi)$) decrease with cumulative values of the Hartman number (Ha). Therefore, the Hartman number is decisive for inducing surface-layer momentum, by which surface shear stress can be controlled. Figure 13 shows the inverse consequence for the Jeffrey fluid's temperature ($\theta(\xi)$). In non-appearance of the Hall effect ($m = 0$), the velocity field is inferior to the Hall effect. Figure 14 shows the radial velocity ($f'(\xi)$) (by varying m), with a significant upsurge in $f'(\xi)$ with m. The reason for this is that the parameter m appears in the denominator of the Lorentz force term in the momentum equation (see Equation (17)), so the larger the m values, the smaller the Lorentz force. As a result, the velocity ($f'(\xi)$) reduces for larger m values. A similar tendency was observed for the azimuth velocity ($g(\xi)$) (see Figure 15). However, the effect of m on the axial velocity ($f(\xi)$) and temperature ($\theta(\xi)$) was insignificant, so it is not presented here.

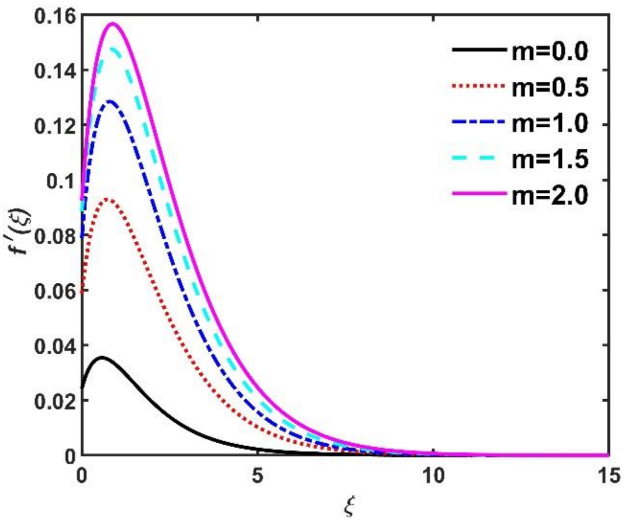

Figure 14. Impact of m on $f'(\xi)$.

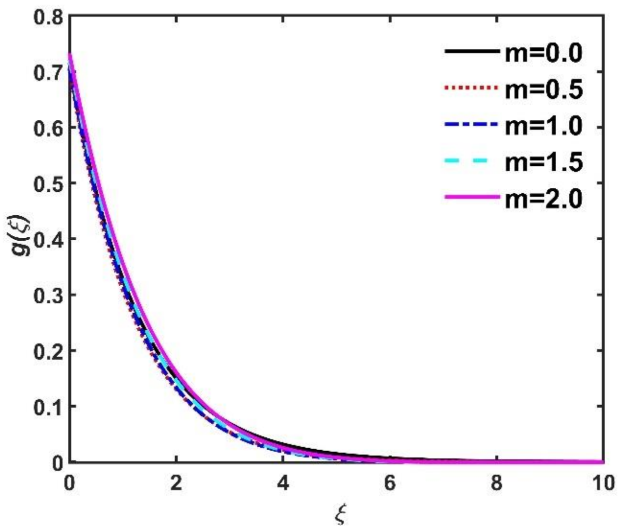

Figure 15. Impact of m on $g(\xi)$.

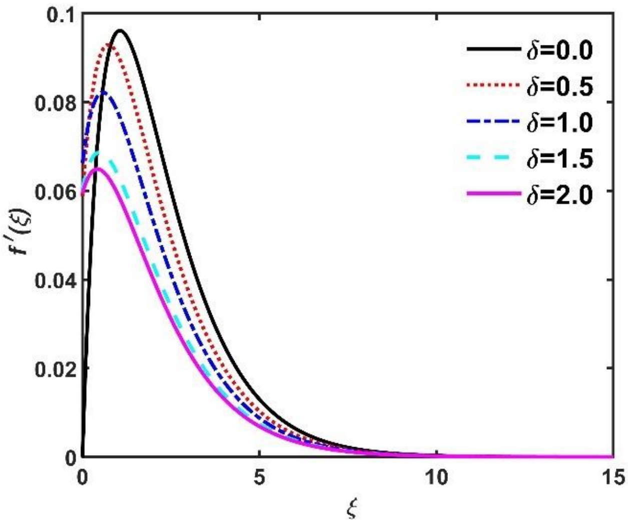

Figure 16. Impact of δ on $f'(\xi)$.

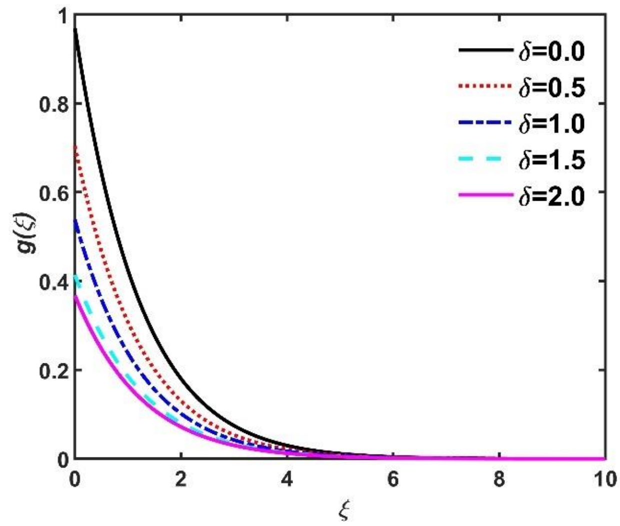

Figure 17. Impact of δ on $g(\xi)$.

Figures 16–18 illustrate the radial velocity ($f'(\xi)$), azimuth velocity ($g(\xi)$), and axial velocity ($f(\xi)$) values for the varying velocity slip factor (δ). The velocity configurations were condensed by the velocity slip factor. It is evident that variation of the radial velocity ($f'(\xi)$) and azimuth velocity ($g(\xi)$) is more substantial in the vicinity of the disk, compared to the rest of the flow domain. This is because of the effectiveness of the slippage on the surface of the disk. Zero slippage within the system creates increased velocity at the surface layer. The thermal configurations ($\theta(\xi)$) in Figure 19 are diminished by the thermal jump factor (ζ). Figures 20 and 21 show how the TRHS and ERHS factors affect the thermal configurations ($\theta(\xi)$), and they also present a comparison of the TRHS and ERHS phenomena. The thermal configurations ($\theta(\xi)$) are heightened by the large TRHS and ERHS factors. The temperature of the fluid increases, along with Qt and Qe, and the thermal surface layer widens. In comparison, the ERHS process is more effective than the TRHS process. The dispersion of the temperature profile ($\theta(\xi)$) appears to increase as R decreases (see Figure 22). The cumulative radiative heat flux exerts heat in the Jeffrey fluid through electromagnetic waves. This accounts for enlargement in $\theta(\xi)$ subjected to R.

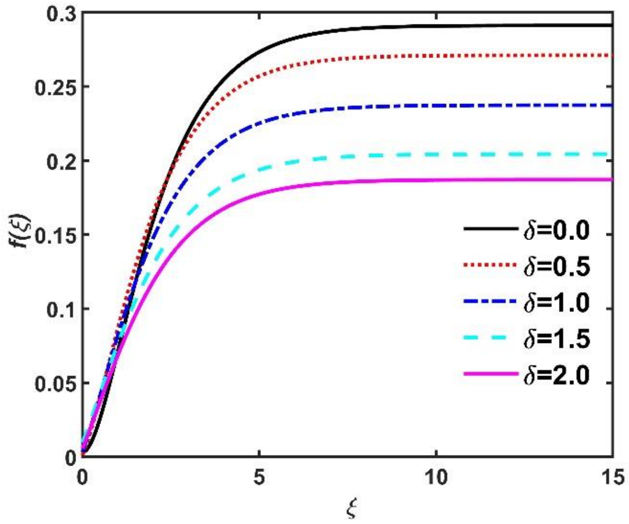

Figure 18. Impact of δ on $f(\xi)$.

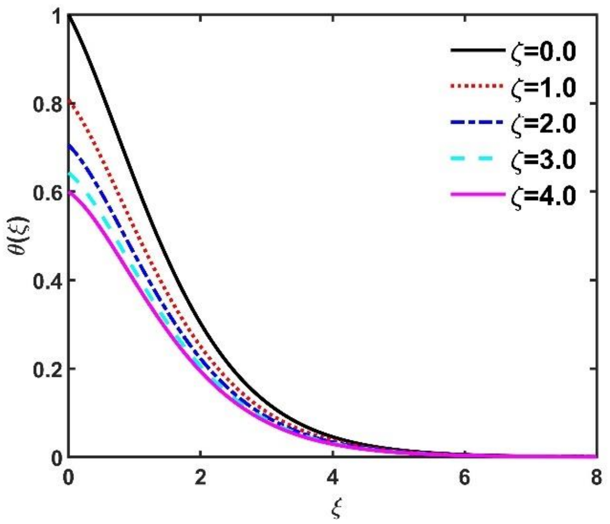

Figure 19. Impact of ζ on $\theta(\xi)$.

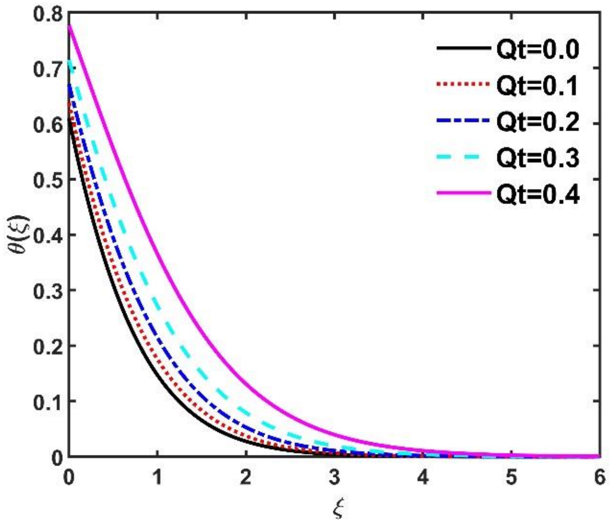

Figure 20. Impact of Qt on $f(\xi)$.

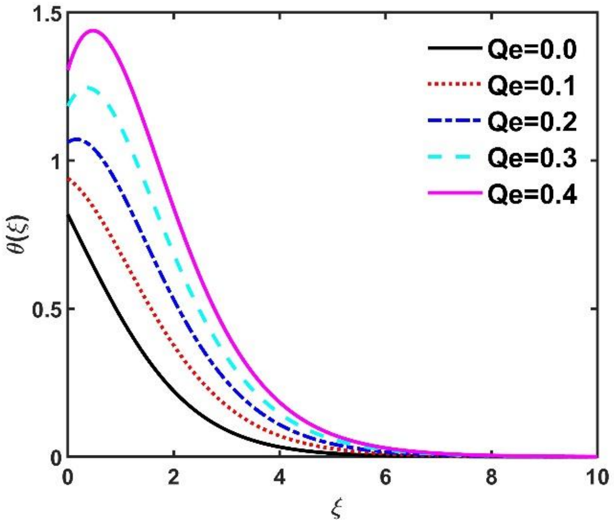

Figure 21. Impact of Qe on $\theta(\xi)$.

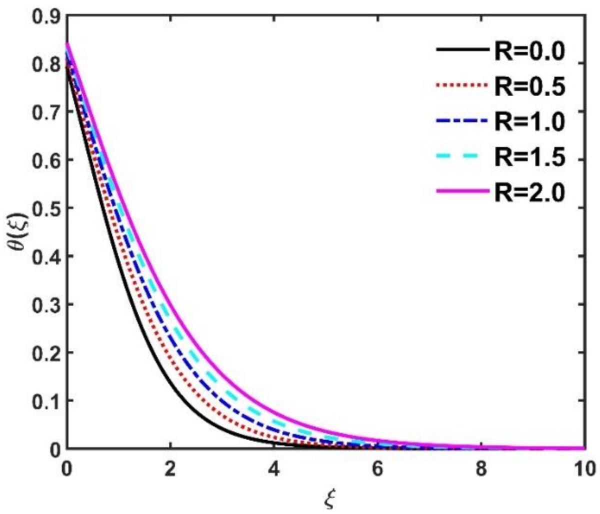

Figure 22. Impact of R on $\theta(\xi)$.

The effect of α and β on the radial shear stress $(\frac{Re_r}{2})^{\frac{1}{2}}C_f$, azimuth shear stress $(\frac{Re_r}{2})^{\frac{1}{2}}C_g$, and Nusselt number $(\frac{Re_r}{2})^{-\frac{1}{2}}Nu$ for a non-magnetic case is shown in Table 2. Here, $(\frac{Re_r}{2})^{\frac{1}{2}}C_f$, $(\frac{Re_r}{2})^{-\frac{1}{2}}Nu$, and $(\frac{Re_r}{2})^{\frac{1}{2}}C_g$ are the cumulative properties of α when $\beta = 0.2$, while an inverse tendency can be seen for β when $\alpha = 0.2$. Table 3 also presents similar results for magnetized Jeffrey fluid. Moreover, the magnitude of $(\frac{Re_r}{2})^{\frac{1}{2}}C_f$, $(\frac{Re_r}{2})^{\frac{1}{2}}C_g$, and $(\frac{Re_r}{2})^{-\frac{1}{2}}Nu$ is progressive for magnetized Jeffrey fluid ($Ha = 0.5$), compared to non-magnetized Jeffrey fluid ($Ha = 0$). The significance of Ha and m for $(\frac{Re_r}{2})^{\frac{1}{2}}C_f$, $(\frac{Re_r}{2})^{\frac{1}{2}}C_g$, and $(\frac{Re_r}{2})^{-\frac{1}{2}}Nu$ is detailed in Table 4. Increasing Ha values reduced the $(\frac{Re_r}{2})^{\frac{1}{2}}C_f$, $(\frac{Re_r}{2})^{\frac{1}{2}}C_g$, and $(\frac{Re_r}{2})^{-\frac{1}{2}}Nu$ profiles, whereas a contrasting trend was noted for m. Moreover, asymptotic performance of $(\frac{Re_r}{2})^{\frac{1}{2}}C_f$, $(\frac{Re_r}{2})^{\frac{1}{2}}C_g$, and $(\frac{Re_r}{2})^{-\frac{1}{2}}Nu$ was observed for larger values of m. That is, the effect of the Lorentz force was negligible when $m = 100$ (sufficiently large).

Table 2. The values of $(\frac{Re_r}{2})^{\frac{1}{2}}C_f$, $(\frac{Re_r}{2})^{\frac{1}{2}}C_g$, and $(\frac{Re_r}{2})^{-\frac{1}{2}}Nu$ for different values of α and β by setting $R = 0.5,\ m = 1,\ \delta = \zeta = 0.5,\ \Gamma = 0.1,\ Qt = Qe = 0.2$, $Pr = 6$, and $n = 1$.

Ha	α	β	Non-Magnetic Jeffrey Fluid		
			$(\frac{Re_r}{2})^{\frac{1}{2}}C_f$	$(\frac{Re_r}{2})^{\frac{1}{2}}C_g$	$(\frac{Re_r}{2})^{-\frac{1}{2}}Nu$
	0.1	0.2	−0.06125664	−0.39446355	−1.17901854
	0.2	0.2	−0.06008768	−0.37373903	−1.17861751
	0.3	0.2	−0.05897289	−0.35550976	−1.17834275
	0.4	0.2	−0.05790908	−0.33932084	−1.17817031
0.0	0.5	0.2	−0.05689318	−0.32482506	−1.17808173
	0.2	0.1	0.05340656	−0.35924537	−1.15292255
	0.2	0.2	−0.06008768	−0.37373903	−1.17861751
	0.2	0.3	−0.17308504	−0.38369116	−1.18436835
	0.2	0.4	−0.28369392	−0.39065929	−1.18990441
	0.2	0.5	−0.39113367	−0.39493977	−1.19520976

Table 3. The values of $(\frac{Re_r}{2})^{\frac{1}{2}}C_f$, $(\frac{Re_r}{2})^{\frac{1}{2}}C_g$, and $(\frac{Re_r}{2})^{-\frac{1}{2}}Nu$ for different values of α and β by setting $R = 0.5,\ m = 1,\ \delta = \zeta = 0.5,\ \Gamma = 0.1,\ Qt = Qe = 0.2$, $Pr = 6$, and $n = 1$.

Ha	α	β	Magnetic Jeffrey Fluid		
			$(\frac{Re_r}{2})^{\frac{1}{2}}C_f$	$(\frac{Re_r}{2})^{\frac{1}{2}}C_g$	$(\frac{Re_r}{2})^{-\frac{1}{2}}Nu$
	0.1	0.2	−0.20719834	−0.54699975	−1.21448688
	0.2	0.2	−0.19735447	−0.51658603	−1.21487245
	0.3	0.2	−0.18864641	−0.48992375	−1.21530051
	0.4	0.2	−0.18087120	−0.46631856	−1.21575914
0.5	0.5	0.2	−0.17387347	−0.4452424	−1.21623946
	0.2	0.1	−0.03462087	−0.50858416	−1.18607258
	0.2	0.2	−0.19735447	−0.51658603	−1.21487245
	0.2	0.3	−0.35766588	−0.51886684	−1.22226033
	0.2	0.4	−0.51393502	−0.5172768	−1.22949732
	0.2	0.5	−0.66511655	−0.51213728	−1.23656366

Table 4. The values of $(\frac{Re_r}{2})^{\frac{1}{2}}C_f$, $(\frac{Re_r}{2})^{\frac{1}{2}}C_g$, and $(\frac{Re_r}{2})^{-\frac{1}{2}}Nu$ for different values of Ha and m by setting $R = 0.5,\ \alpha = \beta = 0.2,\ \delta = \zeta = 0.5,\ \Gamma = 0.1,\ Qt = Qe = 0.2$, $Pr = 6$, and $n = 1$.

Ha	m	$(\frac{Re_r}{2})^{\frac{1}{2}}C_f$	$(\frac{Re_r}{2})^{\frac{1}{2}}C_g$	$(\frac{Re_r}{2})^{-\frac{1}{2}}Nu$
0	0	−0.06008768	−0.37373903	−1.17861751
0.1		−0.08426340	−0.38368352	−1.18984404
0.2		−0.10745435	−0.39453821	−1.20053417
0	5	−0.06008768	−0.37373903	−1.17861751
0.1		−0.06146400	−0.3789904	−1.17769753
0.2		−0.06279512	−0.38411897	−1.17681152
0	10	−0.06008768	−0.37373903	−1.17861751
0.1		−0.06056089	−0.37636651	−1.17802761
0.2		−0.06102613	−0.37896354	−1.17744919
0	100	−0.06008768	−0.37373903	−1.17861751
0.1		−0.06011372	−0.37399731	−1.17854714
0.2		−0.06013971	−0.37425529	−1.1784769

Table 5 presents the $(\frac{Re_r}{2})^{-\frac{1}{2}}Nu$ values for dissimilar values of n, ζ, and R when $\alpha = \beta = 0.2$, $\delta = 0.5$, $\Gamma = 0.1$, $Pr = 6$, and $n = 1$. In the presence of TRHS and ERHS phenomena ($Qt = Qe = 0.2$), the magnitude of $(\frac{Re_r}{2})^{-\frac{1}{2}}Nu$ was found to be greater than when the TRHS and ERHS phenomena were absent ($Qt = Qe = 0$). Furthermore, for increasing values of n and ζ, a substantial increase in $(\frac{Re_r}{2})^{-\frac{1}{2}}Nu$ was observed, whereas a deterioration in $(\frac{Re_r}{2})^{-\frac{1}{2}}Nu$ was seen for rising values of the radiation number (R). Table 6 shows that non-Fourier heat flux is significant in improving heat transport $(\frac{Re_r}{2})^{-\frac{1}{2}}Nu$. That is, $(\frac{Re_r}{2})^{-\frac{1}{2}}Nu$ was found to be higher in the non-Fourier heat flux case than with the Fourier heat flux model.

Table 5. The values of $(\frac{Re_r}{2})^{-\frac{1}{2}}Nu$ for different values of n, ζ, and R by setting $\alpha = \beta = 0.2,\ \delta = 0.5$, $\Gamma = 0.1$, $Pr = 6$, and $n = 1$.

n	ζ	R	$(\frac{Re_r}{2})^{-\frac{1}{2}}Nu$	$(\frac{Re_r}{2})^{-\frac{1}{2}}Nu$
			Qt = Qe = 0.2	**Qt = Qe = 0**
0.1	0.5	0.5	−1.41850538	−1.16647540
0.2			−1.36654000	−1.16647540
0.3			−1.32706867	−1.16647540
0.4			−1.29593067	−1.16647540
1	0.1	0.5	−1.41494968	−1.41884553
	0.2		−1.34453339	−1.34604109
	0.3		−1.28525897	−1.28034291
	0.4		−1.23467631	−1.22075960
1	0.5	0.1	−0.86416390	−0.82476824
		0.2	−0.94531928	−0.90931794
		0.3	−1.02685975	−0.99449018
1	0.5	0.4	−1.10876180	−1.08022592

Table 6. The values of $(\frac{Re_r}{2})^{-\frac{1}{2}}Nu$, for different values of Qe and Qt by setting $R = 0.5,\ n = 1,\ \zeta = 0.5,\ \alpha = \beta = 0.2,\ \delta = 0.5$, $Pr = 6$, and $n = 1$.

Qt	Qe	$(\frac{Re_r}{2})^{-\frac{1}{2}}Nu$	$(\frac{Re_r}{2})^{-\frac{1}{2}}Nu$
		Γ = 0	**Γ = 0.1**
0	0.2	−1.48401825	−1.48133282
−0.1		−1.30346759	−1.30280458
−0.2		−1.19102030	−1.19080604
−0.3		−1.11064431	−1.11056507
−0.2	0	−0.98769763	−0.98736978
	0.1	−1.08935897	−1.08908791
	0.2	−1.19102030	−1.19080604
−0.2	0.3	−1.29268164	−1.29252360

5. Concluding Remarks

Three-dimensional thermal transport of Jeffrey fluid via a gyrating disk was investigated in this study, taking into consideration non-Fourier thermal flux, the ERHS, TRHS, and Hall current. A framework of multiple slip effects was employed. The main results of the analysis are as follows:

- Non-dimensional radial velocity $f'(\xi)$, azimuth velocity $g(\xi)$, and tangential velocity $f(\xi)$ components diminished when Ha values increased but improved due to the Hall current.
- Dimensionless azimuth velocity $g(\xi)$ improved because of a larger β.
- The temperature field $\theta(\xi)$ improved when α and β were elevated.
- The Ha number had a constructive impact on the temperature field $\theta(\xi)$.
- Multiple slip conditions diminished the radial velocity $f'(\xi)$, azimuth velocity $g(\xi)$, radial velocity $f(\xi)$, and temperature $\theta(\xi)$.
- Compared to TRHS, ERHS had a more pronounced effect on temperature $\theta(\xi)$.
- Dimensionless $(\frac{Re_r}{2})^{\frac{1}{2}}C_f$, $(\frac{Re_r}{2})^{-\frac{1}{2}}Nu$, and $(\frac{Re_r}{2})^{\frac{1}{2}}C_g$ diminished when α increased, but this did not happen when β increased.

Considering the non-Fourier thermal flux theory, the current work has shown several remarkable properties of Jeffrey fluid dynamics and heat transfer, due to the gyrating disk. The shooting algorithm was found to be relatively accurate. The simulation presented here takes into account steady-state flow and heat transfer. Future research could expand on the results of this study by incorporating unsteady flows with nanoparticles.

Funding: This research work was funded by Institutional Fund Projects under grant no. (IFPIP: 1216-130-1443).

Institutional Review Board Statement: Not applicable.

Informed Consent Statement: Not applicable.

Data Availability Statement: Not applicable.

Acknowledgments: This research work was funded by Institutional Fund Projects under grant no. (IFPIP: 1216-130-1443). The author gratefully acknowledges technical and financial support provided by the Ministry of Education and King Abdulaziz University, DSR, Jeddah, Saudi Arabia.

Conflicts of Interest: The author declares no conflict of interest.

References

1. Kármán, T.V. Über laminare und turbulente Reibung. *Z. Angew. Math. Mech.* **1921**, *1*, 233–252. [CrossRef]
2. Brady, J.F.; Durlofsky, L. On rotating disk flow. *J. Fluid Mech.* **1987**, *175*, 363–394. [CrossRef]
3. Cobb, E.C.; Saunders, O.A. Heat transfer from a rotating disk. *Proc. R. Soc. Lond. Series A. Math. Phys. Sci.* **1956**, *236*, 343–351.
4. Benton, E.R. On the flow due to a rotating disk. *J. Fluid Mech.* **1966**, *24*, 781–800. [CrossRef]
5. Tribollet, B.; Newman, J. The Modulated Flow at a Rotating Disk Electrode. *J. Electrochem. Soc.* **1983**, *130*, 2016–2026. [CrossRef]
6. Turkyilmazoglu, M. Nanofluid flow and heat transfer due to a rotating disk. *Comput. Fluids* **2014**, *94*, 139–146. [CrossRef]
7. Ellahi, R.; Tariq, M.H.; Hassan, M.; Vafai, K. On boundary layer nano-ferroliquid flow under the influence of low oscillating stretchable rotating disk. *J. Mol. Liq.* **2017**, *229*, 339–345. [CrossRef]
8. Hayat, T.; Muhammad, T.; Shehzad, S.A.; Alsaedi, A. On magnetohydrodynamic flow of nanofluid due to a rotating disk with slip effect: A numerical study. *Comput. Methods Appl. Mech. Eng.* **2016**, *315*, 467–477. [CrossRef]
9. Aziz, A.; Alsaedi, A.; Muhammad, T.; Hayat, T. Numerical study for heat generation/absorption in flow of nanofluid by a rotating disk. *Results Phys.* **2018**, *8*, 785–792. [CrossRef]
10. Mahanthesh, B.; Lorenzini, G.; Oudina, F.M.; Animasaun, I.L. Significance of exponential space-and ther-mal-dependent heat source effects on nanofluid flow due to radially elongated disk with Coriolis and Lorentz forces. *J. Therm. Anal. Calorim.* **2020**, *141*, 37–44. [CrossRef]
11. Cowling, T.G. *Magnetohydrodynamics*; Wiley Inter Science: New York, NY, USA, 1957.
12. Aboul-Hassan, A.L.; Attia, H.A. Flow due to a rotating disk with Hall effect. *Phys. Lett. A* **1997**, *228*, 286–290. [CrossRef]
13. Acharya, N.; Bag, R.; Kundu, P.K. Influence of Hall current on radiative nanofluid flow over a spinning disk: A hybrid approach. *Phys. E: Low-Dimens. Syst. Nanostructures* **2019**, *111*, 103–112. [CrossRef]
14. Maleque, K.A.; Sattar, M.A. The effects of variable properties and Hall current on steady MHD laminar convective fluid flow due to a porous rotating disk. *Int. J. Heat Mass Transf.* **2005**, *48*, 4963–4972. [CrossRef]
15. Abdel-Wahed, M.; Akl, M. Effect of hall current on MHD flow of a nanofluid with variable properties due to a rotating disk with viscous dissipation and nonlinear thermal radiation. *AIP Adv.* **2016**, *6*, 095308. [CrossRef]
16. Shaheen, N.; Ramzan, M.; Alaoui, M.K. Impact of Hall current on a 3D Casson nanofluid flow past a rotating de-formable disk with variable characteristics. *Arab. J. Sci. Eng.* **2021**, *46*, 12653–12666. [CrossRef]
17. Shehzad, S.; Abbas, Z.; Rauf, A.; Mushtaq, T. Effectiveness of Hall current and thermophysical properties in compressible flow of viscous fluid thorough spinning oscillatory disk. *Int. Commun. Heat Mass Transf.* **2020**, *116*, 104678. [CrossRef]
18. Hayat, T.; Ellahi, R.; Asghar, S. Hall effects on unsteady flow due to non-coaxially rotating disk and a fluid at in-finity. *Chem. Eng. Commun.* **2008**, *195*, 958–976. [CrossRef]
19. Maleque, K.A. Effects of combined temperature- and depth-dependent viscosity and hall current on an unsteady mhd laminar convective flow due to a rotating DISK. *Chem. Eng. Commun.* **2009**, *197*, 506–521. [CrossRef]
20. Turkyilmazoglu, M. Exact solutions for the incompressible viscous magnetohydrodynamic fluid of a porous rotating disk flow with Hall current. *Int. J. Mech. Sci.* **2012**, *56*, 86–95. [CrossRef]
21. Ramzan, M.; Riasat, S.; Zhang, Y.; Nisar, K.S.; Badruddin, I.A.; Ahammad, N.A.; Ghazwani, H.A.S. Significance low oscillating magnetic field and Hall current in the nano-ferrofluid flow past a rotating stretchable disk. *Sci. Rep.* **2021**, *11*, 23204. [CrossRef] [PubMed]
22. Barnoon, P.; Toghraie, D.; Salarnia, M.; Karimipour, A. Mixed thermomagnetic convection of ferrofluid in a porous cavity equipped with rotating cylinders: LTE and LTNE models. *J. Therm. Anal. Calorim.* **2020**, *146*, 187–226. [CrossRef]

23. Cai, W.; Toghraie, D.; Shahsavar, A.; Barnoon, P.; Khan, A.; Beni, M.H.; Jam, J.E. Eulerian-Lagrangian investigation of nanoparticle migration in the heat sink by considering different block shape effects. *Appl. Therm. Eng.* **2021**, *199*, 117593. [CrossRef]
24. Barnoon, P.; Toghraie, D.; Karimipour, A. Application of rotating circular obstacles in improving ferrofluid heat transfer in an enclosure saturated with porous medium subjected to a magnetic field. *J. Therm. Anal. Calorim.* **2020**, *145*, 3301–3323. [CrossRef]
25. Basavarajappa, M.; Bhatta, D. Heat and mass transfer of a molten polymer conveying nanoparticles in a wire coating process with temperature-dependent fluid properties: Optimization using Response surface method. *Int. Commun. Heat Mass Transf.* **2022**, *133*, 105941. [CrossRef]
26. Xiao, C.; Nourbakhsh, M.; Alizadeh, A.; Toghraie, D.; Barnoon, P.; Khan, A. Investigation of thermal behavior and performance of different microchannels: A case study for traditional and Manifold Microchannels. *Case Stud. Therm. Eng.* **2022**, *39*, 102393. [CrossRef]
27. Basavarajappa, M.; Bhatta, D. Unsteady nonlinear convective flow of a nanofluid over a vertical plate due to impulsive motion: Optimization and sensitivity analysis. *Int. Commun. Heat Mass Transf.* **2022**, *134*, 106036. [CrossRef]
28. Miansari, M.; Darvishi, M.R.; Toghraie, D.; Barnoon, P.; Shirzad, M.; Alizadeh, A. Numerical investigation of grooves effects on the thermal performance of helically grooved shell and coil tube heat exchanger. *Chin. J. Chem. Eng.* **2021**, *44*, 424–434. [CrossRef]
29. Akram, S.; Athar, M.; Saeed, K.; Razia, A.; Muhammad, T.; Alghamdi, H.A. Mathematical simulation of double diffusion convection on peristaltic pumping of Ellis nanofluid due to induced magnetic field in a non-uniform channel: Applications of magnetic nanoparticles in biomedical engineering. *J. Magn. Magn. Mater.* **2023**, *569*, 170408. [CrossRef]
30. Akram, S.; Athar, M.; Saeed, K.; Razia, A.; Muhammad, T.; Hussain, A. Hybrid double-diffusivity convection and induced magnetic field effects on peristaltic waves of Oldroyd 4-constant nanofluids in non-uniform channel. *Alex. Eng. J.* **2023**, *65*, 785–796. [CrossRef]
31. Qasim, M. Heat and mass transfer in a Jeffrey fluid over a stretching sheet with heat source/sink. *Alex. Eng. J.* **2013**, *52*, 571–575. [CrossRef]
32. Reddy, M.G.; Makinde, O.D. Magnetohydrodynamic peristaltic transport of Jeffrey nanofluid in an asymmetric channel. *J. Mol. Liq.* **2016**, *223*, 1242–1248. [CrossRef]
33. Sandeep, N.; Sulochana, C.; Animasaun, I.L. Stagnation-Point Flow of a Jeffrey Nanofluid over a Stretching Surface with Induced Magnetic Field and Chemical Reaction. *Int. J. Eng. Res. Afr.* **2015**, *20*, 93–111. [CrossRef]
34. Mehmood, R.; Nadeem, S.; Saleem, S.; Akbar, N.S. Flow and heat transfer analysis of Jeffery nano fluid impinging obliquely over a stretched plate. *J. Taiwan Inst. Chem. Eng.* **2017**, *74*, 49–58. [CrossRef]
35. Saleem, S.; Al-Qarni, M.M.; Nadeem, S.; Sandeep, N. Convective Heat and Mass Transfer in Magneto Jeffrey Fluid Flow on a Rotating Cone with Heat Source and Chemical Reaction. *Commun. Theor. Phys.* **2018**, *70*, 534. [CrossRef]
36. Khan, N.A.; Khan, S.; Riaz, F. Analytic Approximate Solutions and Numerical Results for Stagnation Point Flow of Jeffrey Fluid Towards an Off-Centered Rotating Disk. *J. Mech.* **2014**, *31*, 201–215. [CrossRef]
37. Farooq, M.; Gull, N.; Alsaedi, A.; Hayat, T. MHD Flow of a Jeffrey Fluid with Newtonian Heating. *J. Mech.* **2015**, *31*, 319–329. [CrossRef]
38. Hayat, T.; Qayyum, S.; Imtiaz, M.; Alsaedi, A. Homogeneous-heterogeneous reactions in nonlinear radiative flow of Jeffrey fluid between two stretchable rotating disks. *Results Phys.* **2017**, *7*, 2557–2567. [CrossRef]
39. Reddy, G.B.; Sreenadh, S.; Reddy, R.H.; Kavitha, A. Flow of a Jeffrey fluid between torsionally oscillating disks. *Ain Shams Eng. J.* **2015**, *6*, 355–362. [CrossRef]
40. Hayat, T.; Abbas, T.; Ayub, M.; Muhammad, T.; Alsaedi, A. On Squeezed Flow of Jeffrey Nanofluid between Two Parallel Disks. *Appl. Sci.* **2016**, *6*, 346. [CrossRef]
41. Hayat, T.; Farooq, S.; Ahmad, B.; Alsaedi, A. Effectiveness of entropy generation and energy transfer on peristaltic flow of Jeffrey material with Darcy resistance. *Int. J. Heat Mass Transf.* **2017**, *106*, 244–252. [CrossRef]
42. Muhammad, T.; Hayat, T.; Alsaedi, A.; Qayyum, A. Hydromagnetic unsteady squeezing flow of Jeffrey fluid between two parallel plates. *Chin. J. Phys.* **2017**, *55*, 1511–1522. [CrossRef]
43. Kumar, P.M.; Kavitha, A. Three-dimensional flow of Jeffrey fluid between a rotating and stationary disks with suction. *Ain Shams Eng. J.* **2018**, *9*, 2351–2356. [CrossRef]
44. Hayat, T.; Nawaz, M.; Awais, M.; Obaidat, S. Axisymmetric magnetohydrodynamic flow of Jeffrey fluid over a rotating disk. *Int. J. Numer. Methods Fluids* **2011**, *70*, 764–774. [CrossRef]
45. Siddiqui, A.M.; Farooq, A.A.; Haroon, T.; Babcock, B.S. A variant of the classical von Karman flow for a Jeffrey fluid. *Appl. Math. Sci.* **2013**, *7*, 983–991. [CrossRef]
46. Qasim, M.; Afridi, M.I.; Wakif, A.; Saleem, S. Influence of Variable Transport Properties on Nonlinear Radioactive Jeffrey Fluid Flow Over a Disk: Utilization of Generalized Differential Quadrature Method. *Arab. J. Sci. Eng.* **2019**, *44*, 5987–5996. [CrossRef]
47. Sadiq, M.N.; Sajid, M.; Fahim, M.; Javed, T.; Ali, N. Swirling Flow of Jeffrey Fluid by a Spiraling Disk. *Iran. J. Sci. Technol. Trans. A: Sci.* **2020**, *44*, 821–831. [CrossRef]
48. Imtiaz, M.; Shahid, F.; Hayat, T.; Alsaedi, A. Chemical reactive flow of Jeffrey fluid due to a rotating disk with non-Fourier heat flux theory. *J. Therm. Anal. Calorim.* **2019**, *140*, 2461–2470. [CrossRef]
49. Sadiq, M.; Sajid, M.; Javed, T.; Ali, N. Modeling and simulation for estimating thin film lubrication effects on flow of Jeffrey liquid by a spiraling disk. *Eur. J. Mech.—B/Fluids* **2021**, *91*, 167–176. [CrossRef]
50. Fourier, J. *Théorie Analytique de Chaleur*; Chez firmin didot, pere et fils; Libraries pour les Mathématiques: Paris, France, 1822.

51. Cattaneo, C. Sulla conduzione del calore. *Atti Sem. Mat. Fis. Univ. Modena* **1948**, *3*, 83–101.
52. Christov, C. On frame indifferent formulation of the Maxwell–Cattaneo model of finite-speed heat conduction. *Mech. Res. Commun.* **2008**, *36*, 481–486. [CrossRef]
53. Bissell, J.J. Thermal convection in a magnetized conducting fluid with the Cattaneo–Christov heat-flow model. *Proc. R. Soc. A: Math. Phys. Eng. Sci.* **2016**, *472*, 20160649. [CrossRef] [PubMed]
54. Layek, G.; Pati, N. Bifurcations and chaos in convection taking non-Fourier heat-flux. *Phys. Lett. A* **2017**, *381*, 3568–3575. [CrossRef]
55. Mehmood, R.; Rana, S.; Anwar Bég, O.; Kadir, A. Numerical study of chemical reaction effects in magnetohydro-dynamic Oldroyd-B: Oblique stagnation flow with a non-Fourier heat flux model. *J. Braz. Soc. Mech. Sci. Eng.* **2018**, *40*, 526. [CrossRef]
56. Shamshuddin, M.D.; Mishra, S.R.; Bég, O.A.; Kadir, A. Numerical study of heat transfer and viscous flow in a dual rotating extendable disk system with a non-Fourier heat flux model. *Heat Transf.* **2018**, *48*, 435–459. [CrossRef]
57. Mabood, F.; Mackolil, J.; Mahanthesh, B.; Rauf, A.; Shehzad, S.A. Dynamics of Sutterby fluid flow due to a spinning stretching disk with non-Fourier/Fick heat and mass flux models. *Appl. Math. Mech.* **2021**, *42*, 1247–1258. [CrossRef]
58. Kumar, P.B.S.; Mahanthesh, B.; Gireesha, B.J.; Shehzad, S.A. Quadratic convective flow of radiated nano-Jeffrey liquid subject to multiple convective conditions and Cattaneo-Christov double diffusion. *Appl. Math. Mech.* **2018**, *39*, 1311–1326. [CrossRef]
59. Hayat, T.; Javed, M.; Imtiaz, M.; Alsaedi, A. Effect of Cattaneo-Christov heat flux on Jeffrey fluid flow with variable thermal conductivity. *Results Phys.* **2017**, *8*, 341–351. [CrossRef]